Distribution Agreement

In presenting this thesis as a partial fulfillment of the requirements for a degree from Emory University, I hereby grant to Emory University and its agents the non-exclusive license to archive, make accessible, and display my thesis in whole or in part in all forms of media, now or hereafter now, including display on the World Wide Web. I understand that I may select some access restrictions as part of the online submission of this thesis. I retain all ownership rights to the copyright of the thesis. I also retain the right to use in future works (such as articles or books) all or part of this thesis.

Sabina Iqbal 3/29/23

Opto-Chemogenetic Modulation of Astrocytic Buffering for Re-Establishing Neuronal Homeostasis

by

Sabina Iqbal

Ken Berglund, PhD
Adviser

Neuroscience and Behavioral Biology

Ken Berglund, PhD

Adviser

Anita Devineni, PhD

Committee Member

Keith Easterling, PhD

Committee Member

2023

Opto-Chemogenetic Modulation of Astrocytic Buffering for Re-Establishing Neuronal Homeostasis

by

Sabina Iqbal

Ken Berglund, PhD
Adviser

An abstract of
a thesis submitted to the Faculty of Emory College of Arts and Sciences of Emory University in partial fulfillment of the requirements of the degree of Bachelor of Sciences with Honors

Neuroscience and Behavioral Biology

2023

Abstract:

Astrocytes play an important role in maintaining a stable extracellular environment for neurons, via their maintenance of extracellular potassium ion concentration ($[K^+]_O$) and subsequent diffusion through the astrocytic network. During seizure activity, the excessive efflux of K^+ from neurons causes a series of downstream effects which result in astrocyte alkalization and ultimate uncoupling of astrocyte gap junctions. This biochemical chain reaction in astrocytes leads to deterioration of K^+ uptake and exacerbation of epileptic seizures. To counter these effects, we proposed indirect molecular neuromodulation through hippocampal astrocytes with the novel inhibitory luminopsin iLMO7, which combines the light-activated inward chloride pump halorhodopsin (NpHR) with a bioluminescent luciferase (NanoLuc). Here we explored the ability of iLMO7 to modulate intracellular chloride concentration ($[Cl^-]_i$) and intracellular pH (pH_i) using heterologous expression systems, a human astrocytic cell line and a human embryonic kidney cell line. Both chemical activation of NpHR (via coelenterazine-mediated bioluminescence of NanoLuc) and optical activation (via external light) were analyzed in transfected cells using a plate reader. Two ratiometric fluorescent proteins, SuperClomeleon and pHluorin2, were co-transfected to monitor pertinent changes in $[Cl^-]_i$ and pH_i, respectively, before and after activation of NpHR. Acidification of the astrocyte interior following activation of NpHR indicates potential for a therapeutic treatment by restoring the seizure- and $[K^+]_o$-induced alkalization of astrocytes.

Opto-Chemogenetic Modulation of Astrocytic Buffering for Re-Establishing Neuronal Homeostasis

by

Sabina Iqbal

Ken Berglund, PhD
Adviser

A thesis submitted to the Faculty of Emory College of Arts and Sciences
of Emory University in partial fulfillment
of the requirements of the degree of
Bachelor of Sciences with Honors

Neuroscience and Behavioral Biology

2023

Acknowledgements

Thank you to Dr. Berglund, who has given me endless encouragement, guidance, and support since the first day I became his mentee as a high school student.

Thank you to Matthew Stern, Dr. Claire-Anne Gutekunst, Eric Cole, Henry Skelton, Madison, and Alekhya of the Gross lab for always being willing to lend me a helping hand.

Thank you to Dr. Robert Gross for letting me wreak havoc in his lab for the last five years.

Thank you to my wonderful friends – Richard Lee, Ayla Anderson, Ali Ebada, Hannah Geoffroy, Akash Shanmugam, and Nishant Satapathy – for always being there.

And lastly, thank you to Mamma, Baba, and Adano for the love they have given me my whole life and especially during the last few months.

Table of Contents

Figures and Tables

Introduction

Background

Astrocytes are a glial cell type that play an important role in maintaining a stable extracellular environment for neurons. During neuronal excitation, neurons release potassium ions (K^+) into the extracellular fluid - this outflow must be managed for neuronal cells to continue functioning normally. Astrocytes have exceptional K^+ conductance. Mechanistically, the network of astrocytes surrounding neurons is able to take up released K^+ and pass them through interlocking gap junctions, effectively diffusing the neuronal efflux of positive ions (Wallraff et al. 2006). A buildup of extracellular K^+ can cause an array of neuronal pathologies, including seizure activity. Specifically, the accumulation of positive charge within the astrocyte is harmful, as functional astrocytes are optimized for hyperpolarized conditions.

Within the astrocytes, the increase in K^+ triggers activation of a symporter cotransporter (NBCe1) that brings in sodium (1 Na^+) and bicarbonate ions (2 HCO_3^-). The intracellular bicarbonate ions ultimately create alkali conditions within the astrocytes, with harmful effects: the increase in astrocyte pH closes the gap junctions and decouples the astrocytes, which greatly limits their ability to diffuse excess potassium (Onodera et al. 2021). The accumulation of excess extracellular K^+ is known to exacerbate seizure activity and promote hyperexcitability (Bellot-Saez et al. 2017). Additionally, the alkalization of astrocytes has been shown to co-occur with seizure-like activity in vitro (Raimondo et al 2016). Seizures are the defining characteristic of epilepsy, a neurological disease characterized by two or more unprovoked seizures. Epilepsy affects 1% of the population, and an astounding one-third of epilepsy cases are refractory, or pharmaco-resistant (Fattorusso et al. 2021). Even in cases which are treatable via medication,

side effects can be severe and life-altering for patients. Surgical treatments, including DBS implantation and resective procedures, are invasive for patients. Modern neurological research is increasingly steering towards glial cell-oriented approaches to treatment, thus the proposed astrocytic pathway addressed in this experiment holds promise for the large sub-population affected by refractory epilepsy.

Previous studies (Ruminot et al. 2011, Onodera et al. 2021) have attempted to combat the astrocytic alkalization and subsequent decoupling pharmacologically by using an antagonist or knockout model to block NBC sodium bicarbonate cotransporters. This approach effectively prevented intracellular alkalization and hyperactivity, indicating the potential of this pathway as a means of eventual therapeutic treatment. This being said, NBC cotransporters are involved with astrocytic glycolysis and its modulation in response to synaptic activity. Permanently blockading NBC transporters could lead to metabolic dysregulation and ultimate cell damage and dysfunction. Additionally, blocking NBC transporters runs the risk of overcorrecting against alkalization and ultimately over-acidifying the intracellular astrocytic environment. Over-acidification of astrocytes has also been shown to decouple astrocyte gap junctions (Swietach et al. 2007). Thus, there is a need for a novel approach to intervention along the promising astrocyte de-coupling pathway.

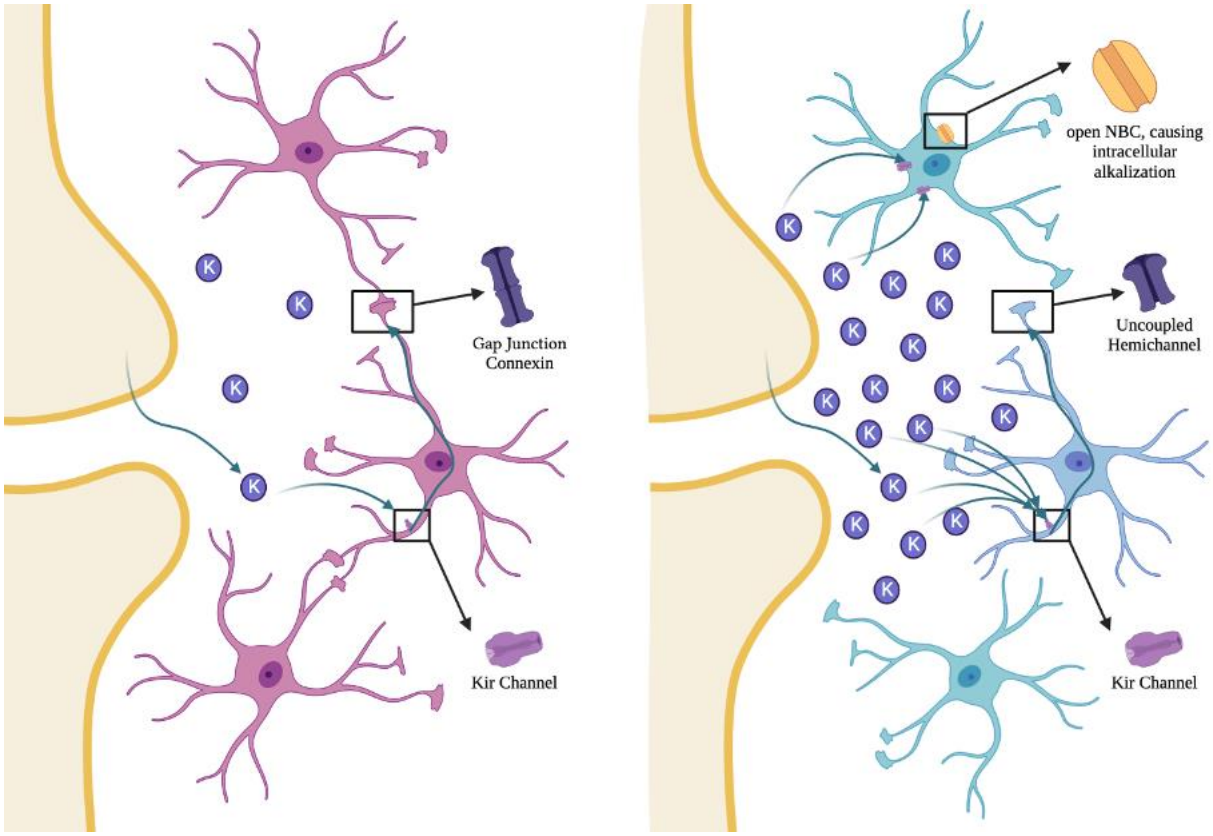

Figure 1 *– A depiction of the tripartite synapse, with emphasis on surrounding astrocytes. The image on the left shows normal astrocytic spatial buffering of potassium ions via gap junctions. The figure on the right shows a system exhibiting neuronal hyperactivity, which causes an increased release of potassium ions into the extracellular space. These potassium ions are taken up by astrocytes and lead to depolarization, alkalization, and decoupling of the astrocytic network. Image produced via BioRender*

Other studies have attempted to use optogenetics to alter pH and maintain hyperpolarization in astrocytes. Mice were treated to express NpHR (*Natronomonas* halorhodopsin; Gradinaru et al. 2008) with photostimulation. NpHR is a chloride ion (Cl^-) pump that brings Cl^- into the astrocyte to maintain hyperpolarized conditions. Increasing intracellular Cl^- concentration ($[Cl^-]_i$) has been shown to lower $[K^+]_o$, although the cellular mechanism by

which this occurs is not yet well-understood; EbrahimAmini et al. 2021 found that photostimulation of NpHR-expressing astrocytes decreased $[K^+]_o$. Another study (Tonnesen et al. 2009) found that NpHR photostimulation in the hippocampal region of mice suppressed seizure activity. These studies offer promising results for membrane proteins that can aid in the maintenance of hyperpolarized astrocytic conditions.

Hypothesis and Goals

This project posits the use of the inhibitory luminopsin iLMO7 to maintain hyperpolarized conditions in astrocytes. iLMO7 is a chimeric protein that couples a bioluminescent protein (NanoLuc) to a light-sensitive opsin (NpHR). This particular luminopsin can be activated both optically and chemically. In response to external light (optical stimulation), the opsin pumps Cl^- into the intracellular space. Systemic administration of a luciferin (chemical stimulation) causes emission of light via chemical reaction with the bioluminescent protein, and this light also subsequently stimulates the opsin. In contrast to prior optogenetic approaches, this fusion protein offers a tight, closed-loop approach by using the chemical bioluminescent moiety as a source of light. This approach also minimizes invasiveness compared to other methods of photo-stimulation by allowing for hybridized chemo-optogenetic stimulation. Previously, we have utilized iLMO2 (Tung et al. 2015) as an inhibitory luminopsin of choice. Comparatively, iLMO7 utilizes mNeonGreen (Shaner et al. 2013) instead of Venus YFP, and NanoLuc instead of *Renilla* luciferase (Figure 1.1). These substitutions are expected to yield greater fluorescence and bioluminescence, thus conferring more robust effects of chemo-optogenetics. A bioluminescence assay will be utilized to explore this further.

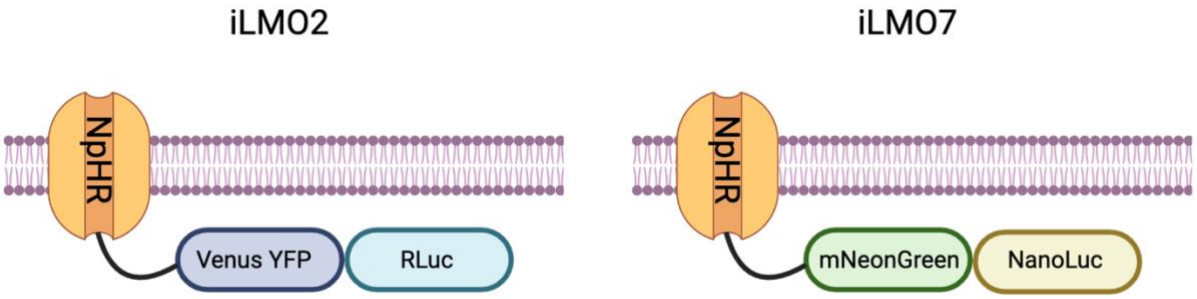

Figure 1.1 *- Image showing the differing components between iLMO7 (our novel protein) and iLMO2 (a previously utilized optogenetic protein). Venus YFP and mNeonGreen are fluorescent proteins used to confirm expression. RLuc and NanoLuc are the bioluminescent components. Both contain the NpHR inward Cl^- pump. Image produced via BioRender*

In addition to the bioluminescence assays, two additional analyses will be carried out to analyze downstream cellular effects of iLMO7 expression. First, we will utilize SuperClomeleon (SCLM) to monitor changes in $[Cl^-]_i$ over time after activation of iLMO7. SCLM is a ratiometric fluorescent protein pair that can be transfected into cells to allow for visualization of Cl^- (Herstel et al. 2022). Comparing fluorescence readouts before and after activation of NpHR will help elucidate whether there is a significant influx of Cl^-, which would help counteract the harmful initial depolarization detailed above. Next, we will utilize pHluorin2, another ratiometric fluorescent protein that is sensitive to changes in pH. By measuring fluorescence readouts before and after activation of NpHR, we can monitor any changes in pH over time. A decrease in pH would indicate a potential to counteract the harmful intracellular alkalization within over-active astrocytes.

We will study these effects in both U373 cells (a glioblastoma cell line with astrocytic morphology) and HEK293FT cells (known to have high rates of successful transfection). Since U373 cells mimic astrocytic conditions more closely, we are interested to see how iLMO7 functions in U373 as compared to HEK293FT cells. We will also compare iLMO7 to iLMO2, to evaluate whether iLMO7 is truly a "new and improved" version of the chimeric opsin protein. The desired genetic sequences will be delivered to cells via plasmid vector transfection. Two vectors will be utilized: pcDNA3, a general mammalian expression vector, and pAAV GFAP (glial fibrillary acidic protein) which is intended to target astrocytes. We expect the GFAP vector to have greater expression in the U373 cell line. Cell-based assay data will be collected via a Cytation5 plate reader. We also tested a recombinant adeno-associated viral (AAV) vector derived from pAAV GFAP in mice for an exploratory analysis of iLMO7 expression in astrocytes in vivo.

Results - Bioluminescence

U373 and HEK293FT cells were passaged onto a 96-well plate and incubated for 48 hours prior to transfection by Lipofectamine 3000 (Invitrogen). Control conditions included a non-transfected column, as well as a vector-only column (pcDNA3 only; GFAP vector unavailable). Test conditions included transfection with iLMOx (where x = 7 or 2, corresponding to iLMO7 or iLMO2), and mutated iLMOx (iLMOx RA/SA/DN). The mutated form, iLMOx RA/SA/DN, incorporates three critical loss-of-function point mutations within the inward chloride pump passageway of NpHR (Figure 2b, 2c). This is intended to act as an ideal control

for the downstream effects of iLMOx expression, as only the flow of chloride ions is altered in this condition.

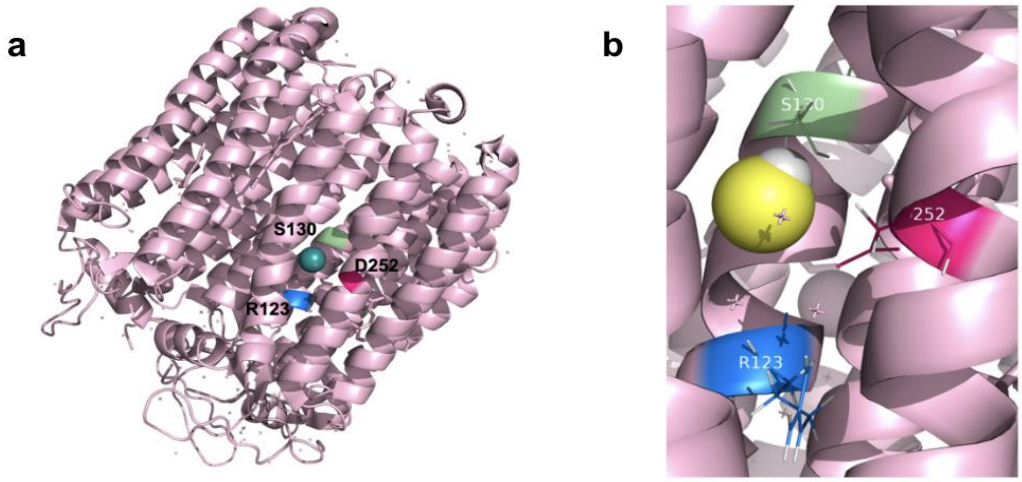

Figure 2 *- The mutated control, iLMOx RA/SA/DN*

a) 3D model of chloride pump NpHR (halorhodopsin). Within the protein, the three residues that have been highlighted (R123 (green), S130 (blue), D252 (pink)) are those which are undergoing point mutations (R123A, S130A, D252N). These residues have been identified as critical for transport of chloride (dark teal, round). b) An alternate, closer look at the area of interest (chloride is yellow). This image was generated using PyMOL (PDB: 3A7K, Chen et al. 2016).

For this assay, the fluorescence of the protein's fluorescent component (mNeonGreen vs. Venus YFP) was measured to compare rates of transfection, by allowing for visualization of iLMOx expression. We would expect no difference in fluorescence between iLMOx and the mutated form iLMOx RA/SA/DN, as mutations to the inward chloride pump area would not affect the fluorescent protein component. Next, bioluminescence from the luciferase component (NanoLuc vs. *Renilla* luciferase) was measured. This should also be unaffected by the

RA/SA/DN mutation. Bioluminescence was activated in live cells through administration of coelenterazine (CTZ), a chemical luciferase substrate.

Following transfection, cells were incubated overnight to allow time for uptake and expression of genetic material. Once an initial fluorescence reading was taken by the Cytation5 plate reader, cell media was replaced with media containing CTZ. Within five minutes, a luminescence measurement was taken by the Cytation5 plate reader.

In HEK cells, iLMO7 has more robust fluorescence, while iLMO2 has more robust luminescence.

Using HEK293FT cells, pcDNA3 iLMO7 and pcDNA3 iLMO2 bioluminescence was analyzed. Use of a common pcDNA3 vector limited confounds for comparison between the two. As expected, there was significantly higher fluorescence in the iLMOx and iLMOx RA/SA/DN transfected cells (Figure 3d) as compared to control conditions. This indicates efficacy of transfection. That being said, greater fluorescence was measured in the iLMO7 species, which utilize mNeonGreen. iLMO2 encodes Venus YFP, thus indicating that mNeonGreen is in fact a more robust GFP for use in chimeric opsin proteins.

Luminescence was significantly higher in iLMOx and iLMOx RA/SA/DN expressing cells compared to control conditions, which is further evidence for successful transfection. In contrast to fluorescence, however, luminescence was found to be higher in HEK 293FT cells expressing iLMO2 compared to those expressing iLMO7. In iLMO7, the bioluminescent enzyme is NanoLuc, while iLMO2 encodes *Renilla* luciferase. Based on the results in figure 3e, *Renilla*

luciferase is the more robust of the two. This is highly important for the subsequent activation of NpHR, which relies on light emitted by the luciferase for its light-dependent pump activation.

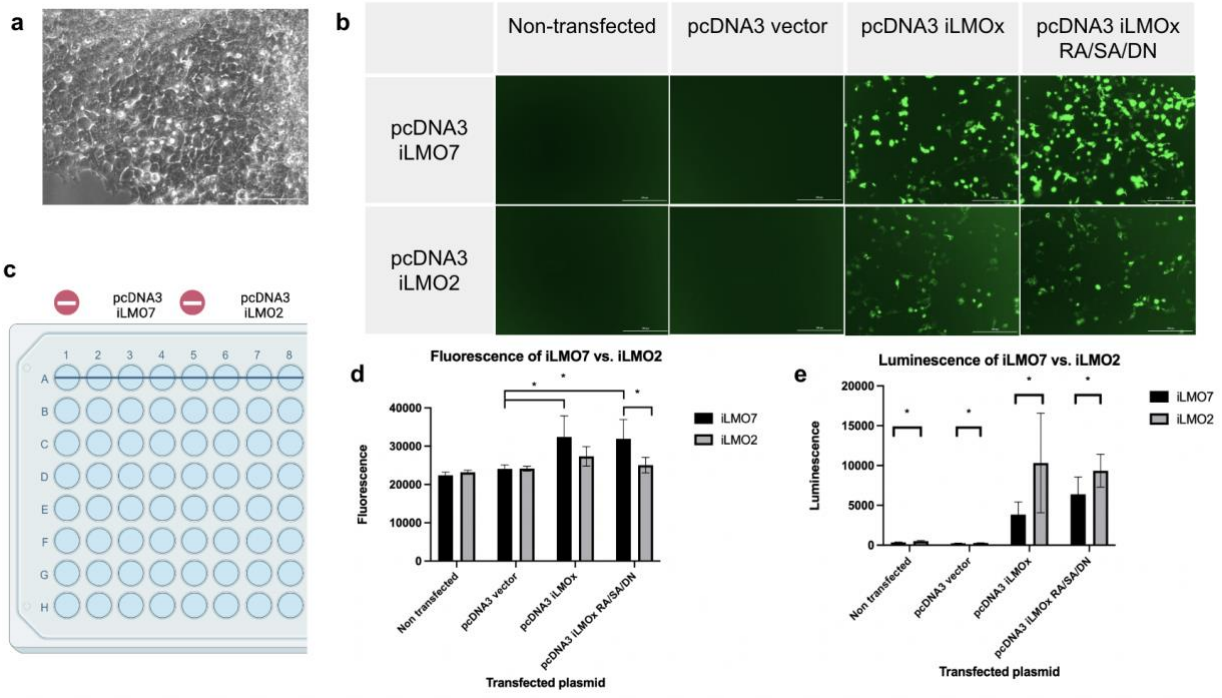

Figure 3 *- Comparing bioluminescence of iLMO7 vs. iLMO2 in HEK293FT Cells*

a) Phase contrast image of HEK 293FT cells at 20X magnification. b) GFP fluorescence images at 20X magnification show fluorescence of mNeonGreen/Venus YFP for each condition. c) Plate setup for comparison between iLMO7 and iLMO2 - columns 1 and 5 were non-transfected. Columns 2 and 6 were transfected with pcDNA3 vector only. Columns 3 and 4 were transfected with pcDNA3 iLMO7 and pcDNA3 iLMO7 RA/SA/DN, respectively. Columns 7 and 8 were transfected with pcDNA3 iLMO2 and pcDNA3 iLMO2 RA/SA/DN, respectively. Image produced via BioRender. d) Graph of fluorescence, comparing iLMO7 and iLMO2. Statistical significance was found using an unpaired t-test with significance level of p = 0.05. e) Graph of luminescence,

comparing iLMO7 and iLMO2. Statistical significance was found using an unpaired t-test with significance level of p = 0.05.

Expression and bioluminescent readings are weaker in transfected U373 cells.

Equivalent experiments were carried out within the U373 glioblastoma cell line. To eliminate confounds, the same batches of freshly-made lipofection cocktails used in the HEK cell trials were also utilized to transfect the U373 cells. However, there were no significant differences among fluorescence readings in U373 cells (figure 4d). Qualitatively, it is clear from comparing figure 4b to figure 3b that there was lower overall expression in U373 cells. Bioluminescence, on the other hand, was detectable in U373 cells, although the intensity was an order-of-magnitude smaller than in HEK cells (figure 3e). The luminescence data in figure 4e reflects the same trends as those shown in HEK cells (figure 3e): luminescence is more robust in iLMO2, favoring *Renilla* luciferase.

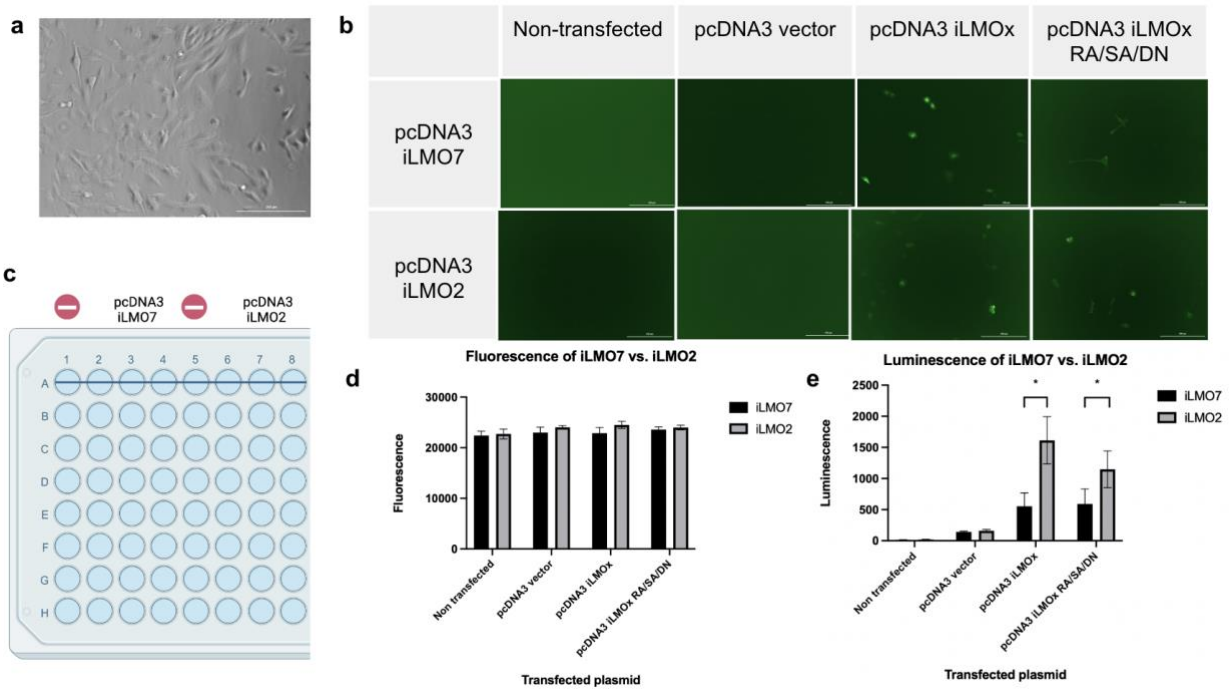

Figure 4 *- Comparing bioluminescence of iLMO7 vs. iLMO2 in U373 Cells*

a) Phase contrast image of U373 cells at 20X magnification. b) GFP fluorescence images at 20X magnification show fluorescence of mNeonGreen/Venus YFP for each condition. c) Plate setup for comparison between iLMO7 and iLMO2 - columns 1 and 5 were non-transfected. Columns 2 and 6 were transfected with pcDNA3 vector only. Columns 3 and 4 were transfected with pcDNA3 iLMO7 and pcDNA3 iLMO7 RA/SA/DN, respectively. Columns 7 and 8 were transfected with pcDNA3 iLMO2 and pcDNA3 iLMO2 RA/SA/DN, respectively. d) Graph of fluorescence, comparing iLMO7 and iLMO2. At a significance level of $p = 0.05$, no significant differences were found for fluorescence readings. e) Graph of luminescence, comparing iLMO7 and iLMO2. Statistical significance was found using an unpaired t-test with significance level of $p = 0.05$.

The GFAP promotor is not effective *in vitro*, as demonstrated by low expression levels.

Glial fibrillary acidic protein (GFAP) is expressed exclusively by astrocytes and is used as a specific marker for the cell type. Thus, the GFAP promotor is expected to target astrocytes for specific expression. In a progression towards a mouse model, this specificity is important to select the correct target cells for treatment. A GFAP iLMO7 transfection cocktail was administered to U373 cells (Figure 5). As a comparison, the same transfection treatments were repeated in non-astrocytic HEK293FT cells (Figure 6). Due to the astrocytic nature of the U373 cell line, we expected higher iLMO7 expression in U373 cells. However, there were low levels of GFAP iLMO7 expression in both cell types. As seen in Figures 5d and 6D, there was no significant difference between fluorescence levels compared to the non-transfected control condition. The luminescence, on the other hand, was significantly higher than control levels in the GFAP iLMO7-transfected U373 cells (Figure 5e), whereas we did not observe significant bioluminescence in GFAP iLMO7-transfected HEK cells (Figure 6E). That being said, the luminescence values were markedly lower than those from pcDNA3 vector-transfected U373 cells (Figure 4e). This points to lower rates of genetic uptake and expression. Thus, the GFAP promoter was able to drive preferential expression of iLMO7 in the astrocytic cell line, although the overall activity of the promoter was somewhat limited compared to the generic, nonspecific cytomegalovirus (CMV) promoter in pcDNA3.

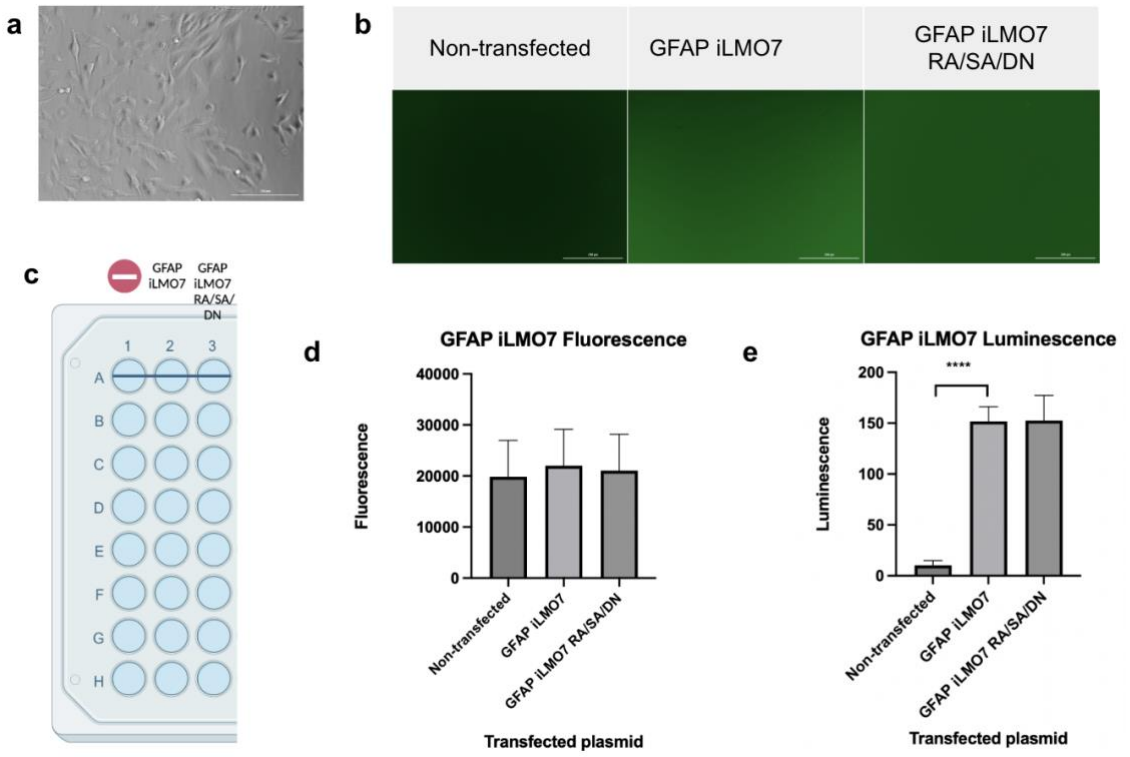

Figure 5 *- GFAP iLMO7 bioluminescence in U373 cells*

a) phase contrast images of cells. b) GFP fluorescence images at 20X magnification show fluorescence of mNeonGreen for each condition. c) Plate setup for GFAP iLMO7 conditions - the first column being a non-transfected control. n = 7 wells per test condition. d) Fluorescence levels across all three conditions. e) Luminescence conditions across the three conditions.

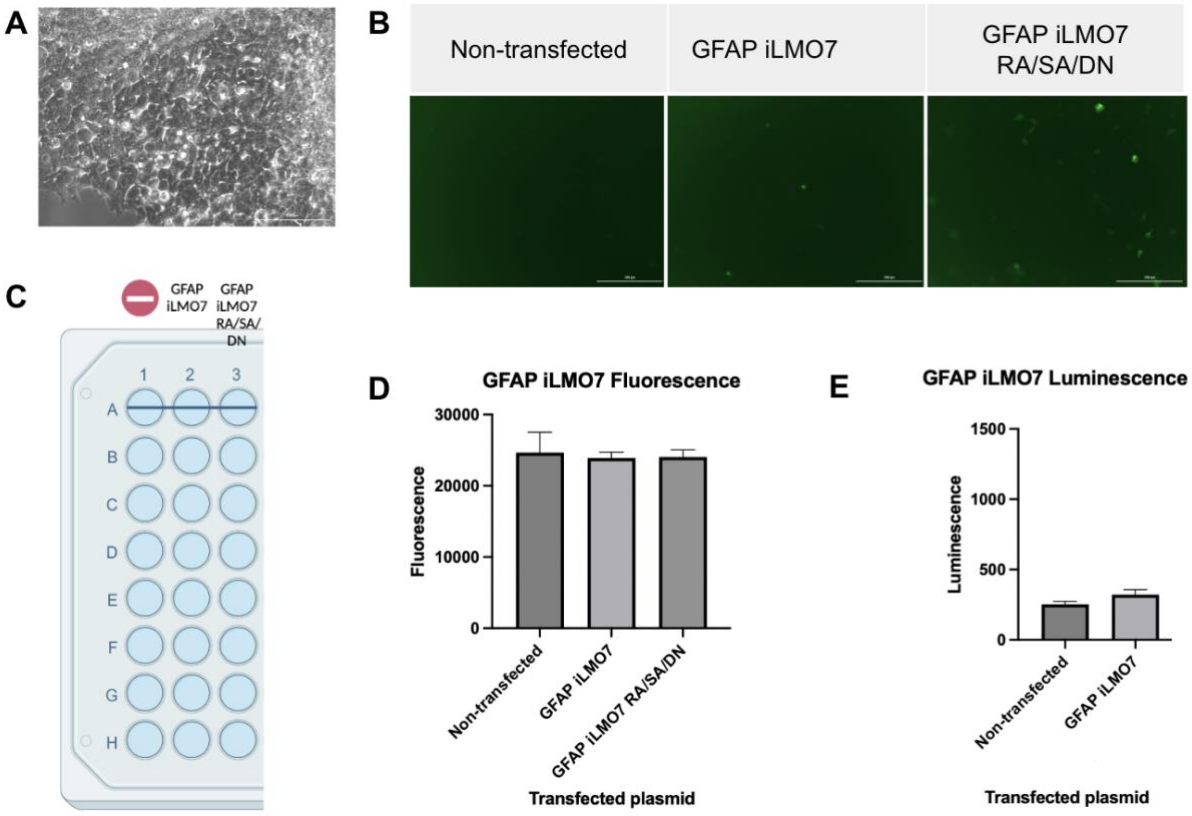

Figure 6 *- GFAP iLMO7 bioluminescence in HEK293FT cells*

A) phase contrast images of cells. B) GFP fluorescence images at 20X magnification show fluorescence of mNeonGreen for each condition. C) Plate setup for GFAP iLMO7 conditions - the first column being a non-transfected control. n = 7 wells per test condition. D) Fluorescence levels across all three conditions. E) Luminescence conditions across the conditions.

Despite weak expression of GFAP *in vitro*, expression of GFAP iLMO7 in mice is high.

We speculate that the low expression levels of iLMO7 in U373 cells is partly due to the incompatible mode of transfection (*i.e.,* lipofection) for this particular cell type. In fact, the

proportion of fluorescent U373 cells was a lot lower than that of fluorescent HEK cells (Figures 3b and 4b). On the other hand, recombinant adeno-associated virus (rAAV) has been used as a very efficient vector for gene delivery *in vitro* as well as *in vivo*. The distinct tropism of rAAV has been utilized to engineer rAAV towards infection in specific cell types, including astrocytes (rAAV.Astro) (Chen et al. 2022). Thus, we bypassed the cell model and utilized an rAAV.Astro vector to administer GFAP iLMO7 to mice. rAAV.Astro was injected intracerebroventricularly within one day after birth. After a wait period of three weeks for adequate expression, mice were anesthetized, injected with CTZ, and monitored for bioluminescence in the brain. As shown in Figure 7d-e, high levels of bioluminescence were observed through the intact skull and skin over time following CTZ injection. This indicates that GFAP iLMO7 in combination with the rAAV.Astro vector was effectively expressed in mice in vivo.

iLMO7 expression in the brain was further examined through immunohistochemical staining (Figure 7a-c). Expression of iLMO7 was confirmed through native fluorescence from the mNeonGreen moiety of iLMO7 while astrocytes were counterstained through GFAP immunoreactivity. DAPI was added for visualization of nuclei. iLMO7 fluorescence appeared as a round ‘haze’ in the neocortex and the hippocampus, consistent with the nature of membrane protein expression in fine processes of astrocytes. Some astrocytes identified through GFAP immunostaining overlapped with iLMO7-driven fluorescence. This confirmed successful expression of iLMO7 specifically in astrocytes in vivo.

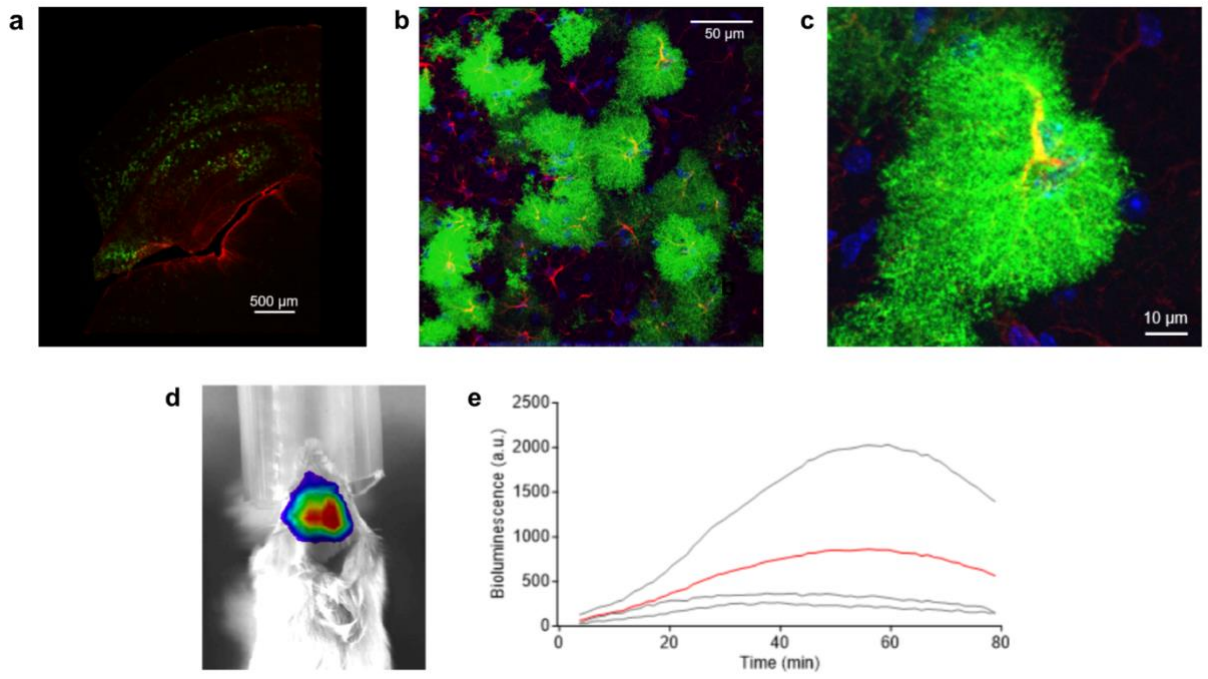

Figure 7 – Mice expressing GFAP iLMO7

a) Coronal cross-section showing the mouse hemisphere including the hippocampus and the neocortex. Red indicates GFAP (astrocytes), green indicates iLMO7, blue indicates DAPI (nuclear marker). Yellow areas indicate overlap of iLMO7 and GFAP. b) higher magnitude image showing branching morphology of GFAP-illuminated projections. c) highest magnitude image, showing overlap of iLMO7 and GFAP. d) Representative image obtained during *in vivo* bioluminescence imaging shown in false color. The head of an albino mouse was shaved and anesthetic gas (isoflurane) was delivered through the plastic tube. e) Bioluminescence over time after CTZ injection. An average (red trace) was derived from three individual mice (gray traces).

Results - Chloride concentration measurements through SCLM

Activation of NpHR in astrocytes with external light has been shown to lower $[K^+]_o$ in the brain (EbrahimAmini et al. 2021). The exact mechanism(s) of this peculiar effect of astrocytic NpHR still need to be elucidated, but we suspect that it involves intricate relationships between K^+, Cl^- and pH, as $[Cl^-]_i$ is coupled with pH_i (Berglund et al. 2015). This, in turn, can affect $[K^+]_o$ as detailed in the introduction. SuperClomeleon (SCLM) is a ratiometric fluorescent protein that acts as an indicator for $[Cl^-]_i$. SCLM includes a chloride-sensitive yellow fluorescent protein (YFP) and a chloride-insensitive cyan fluorescent protein (Cerulean). Mechanistically, binding of Cl^- to the YFP moiety alters the fluorescence resonance energy transfer (FRET) between the FRET donor Cerulean and the FRET acceptor YFP. We quantify these changes as the emission ratio of 541 nm (YFP) over 491 nm (Cerulean) in the heterologous expression systems and a plate reader. Lower FRET ratio indicates greater influx of chloride through the NpHR pump, which is what we hope to see in iLMO7.

We measured the ratio of SCLM-based fluorescence over time, before and after photo stimulation of NpHR through external light. The non-transfected condition exists as a control for autofluorescence. The fluorescence readings from the non-transfected wells were subtracted away from the experimental conditions prior to calculating the SCLM ratios. Our negative control expresses the empty pcDNA3 vector + SCLM only. This baseline condition shows fluorescence without contribution from iLMOx and its associated NpHR pump and GFPs. Lastly, the RA/SA/DN mutant is intended to act as a control for the influx of chloride. We expect to see

a smaller influx of Cl^- in the mutated RA/SA/DN conditions, as compared to non-mutated iLMO7, as the mutations directly affect the inner surface of the chloride transporting pore.

Aside from preparing the optimal controls, another confound that needed to be taken into is photo-bleaching. Photobleaching is a light-induced alteration in fluorophores that limits subsequent fluorescence (Snapp et al. 2003). Prolonged exposure to excitation wavelengths during plate reading caused a general decrease in fluorescence over the course of each well read. Since we are looking for a decrease in FRET ratio, the decrease in fluorescence due to photo-bleaching would illicit falsely positive results. To control for this effect, SCLM ratios were de-trended by subtracting away the slope due to photo-bleaching. Each SCLM-only condition contains every component of the assay except iLMOx and its NpHR pump. Therefore, any change in SCLM-only condition does not reflect a change in chloride, but rather the mere photo-bleaching trend and was subtracted out from every test condition (including its own). The detrended data is graphed in figures 8 and 9.

iLMO7 pumps chloride more effectively than iLMO2 in HEK293FT cells

Figure 8c-d reflect changes in FRET ratio over time for HEK cells, where photo-stimulation is marked by a vertical black line. Figure 8c shows a very significant ($P < 0.01$) drop in FRET ratio for iLMO7, and a significant drop ($p < 0.05$) for iLMO7 RA/SA/DN, as compared to the SCLM-only condition. This drop in FRET ratio signifies an influx of Cl^- after photo-stimulation. The fact that there was no significant decrease in the SCLM-only condition indicates that this influx of Cl^- was due to activation of the NpHR inward chloride pump. Conversely, iLMO2 showed no significant decrease in FRET ratio compared to the SCLM-only condition.

This indicates no significant influx of Cl^- through the NpHR pump of iLMO2. This supports our hypothesis that iLMO7 is a more robust option for mediating neuronal homeostasis.

The RA/SA/DN mutation partially blocks influx of Cl^- through NpHR

As described in the introduction and in Figure 2, the RA/SA/DN mutation affects the inner surface of the chloride pump encapsulated within NpHR. As evidenced by several instances of significant decreases in FRET ratio (Figure 8c, 9c, 9d), the iLMOx RA/SA/DN condition does still allow for passage of Cl^- ions into the cell. Combined with prior literature, this data suggests that RA/SA/DN mutated iLMOx remains partially permeable to Cl^- ions.

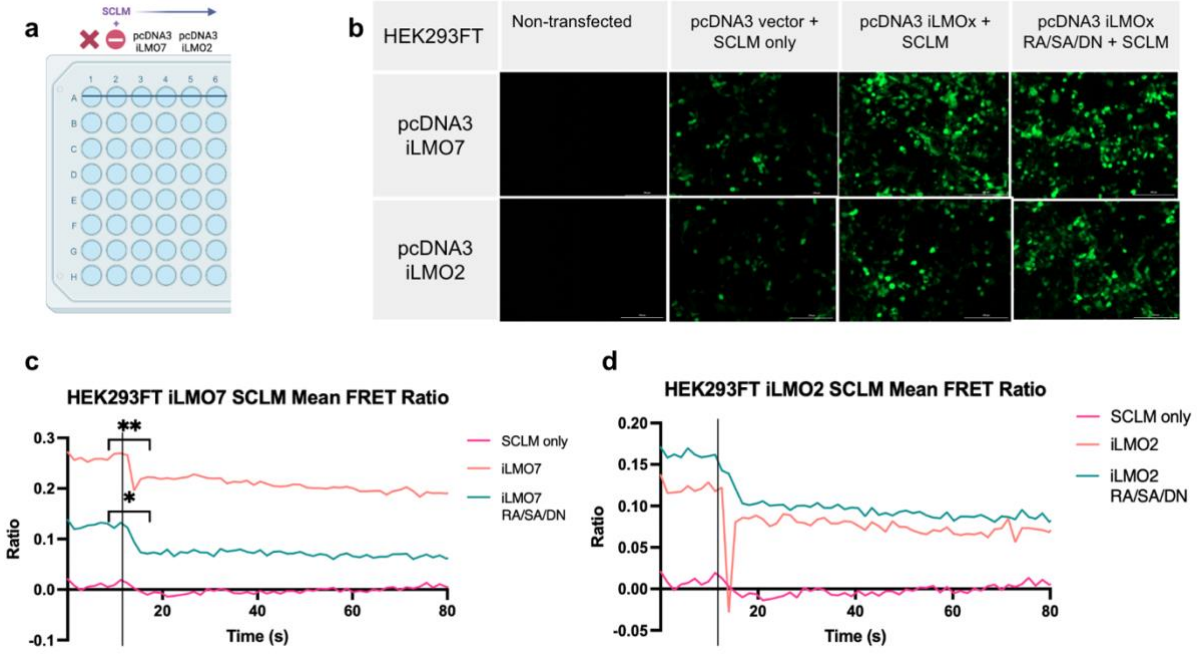

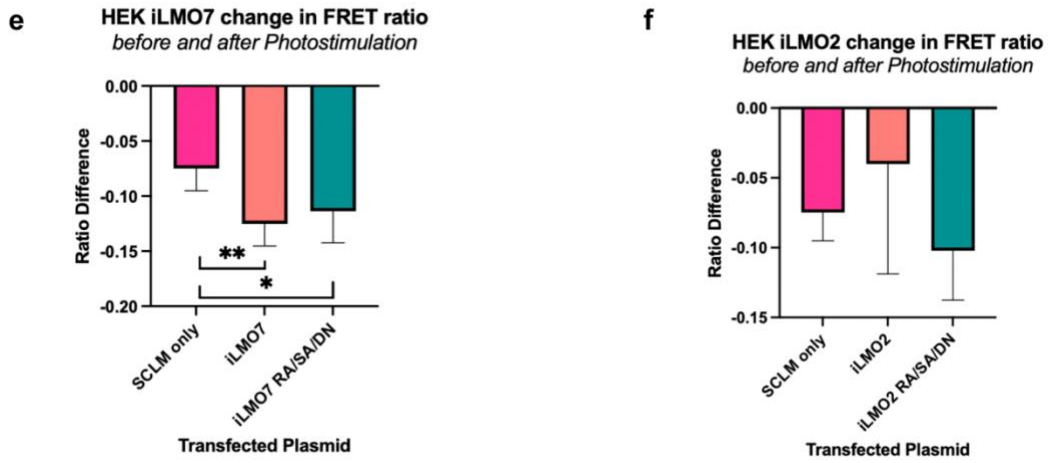

Figure 8 *- HEK293FT SCLM Results, comparing iLMO7 and iLMO2*

a) Plate set-up for HEK 96-well plate expressing SCLM. Column 1 is the non-transfected control, while column 2 is the empty pcDNA3 vector + SCLM only control. Columns 4 and 6 contain the mutated forms of iLMO7 and iLMO2, respectively. n = 7 wells per condition. b) GFP fluorescence images at 10X magnification. c) SCLM ratio for the iLMO7 condition. iLMO7 showed a significant drop in FRET ratio after photo-stimulation (marked by vertical line) compared to the SCLM-only control ($p = 0.003475$, $p< 0.01$). iLMO7 RA/SA/DN also showed a significant drop compared to the SCLM-only control ($p =0.02182$, $p < 0.05$). d) SCLM ratio for the iLMO2 condition. No differences in FRET ratio were significant compared to the SCLM-only control (iLMO2 $p = 0.4745$ ($p > 0.05$), iLMO2 RA/SA/DN $p = 0.6246$ ($p > 0.05$)). e) graph of the differences in FRET ratio before and after photo stimulation for iLMO7. f) graph of the differences in FRET ratio before and after photo stimulation for iLMO2.

The greater efficacy of iLMO7 over iLMO2 is reflected in U373 cells

The results obtained in HEK cells were reflected in U373 cells as well, albeit to a lesser extent. As shown in Figure 9c, both iLMO7 and iLMO7 RA/SA/DN exhibit decreases in FRET

ratio, but non-mutated iLMO7 has a smaller p-value. Both the iLMO7 and iLMO7 RA/SA/DN conditions showed very significant ($p < 0.01$) decreases in FRET ratio in U373 cells (Figure 9c). In comparison, the iLMO2 condition only yielded one significant ($p < 0.05$) decrease (Figure 9d). As we ascertained during the bioluminescence experiments, U373 cells generally exhibit lower rates of expression and fluorescence than HEK293FT cells. This effect is visible in Figure 9c-d as greater noise in the graph. These factors may explain why the differences between conditions are less robust in U373 cells. However, the significant decreases in FRET ratio for iLMO7 conditions further confirm the stronger capabilities of iLMO7 in terms of Cl^- transport.

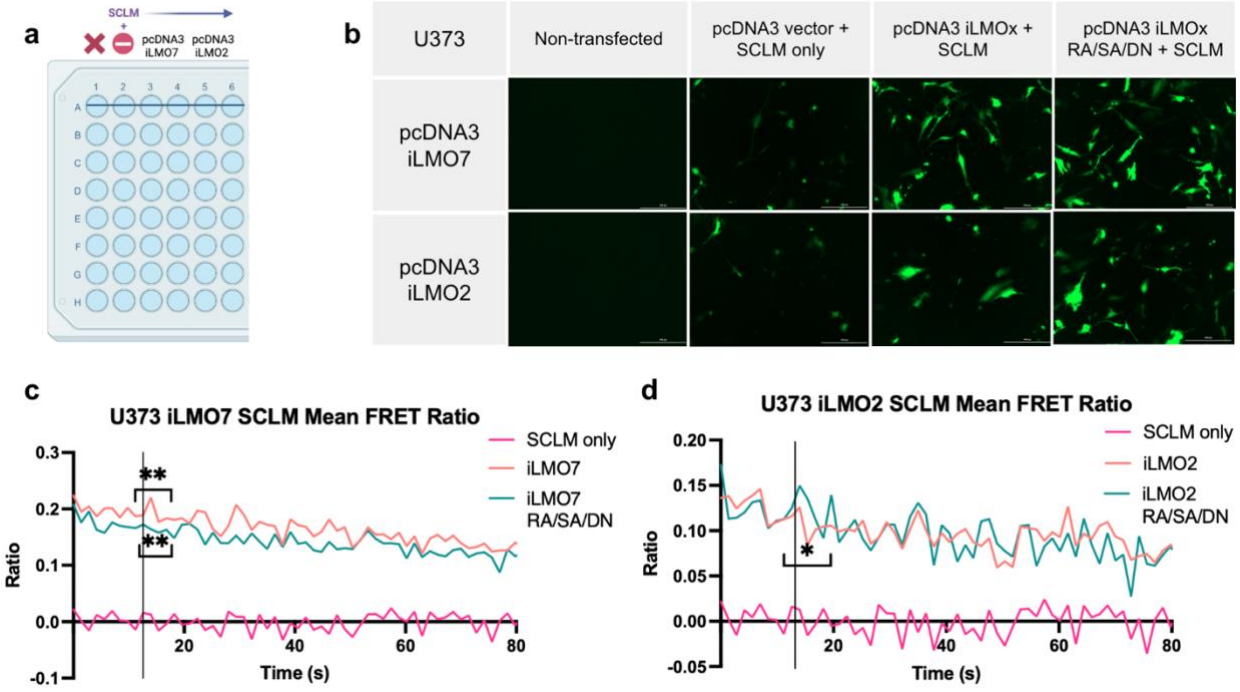

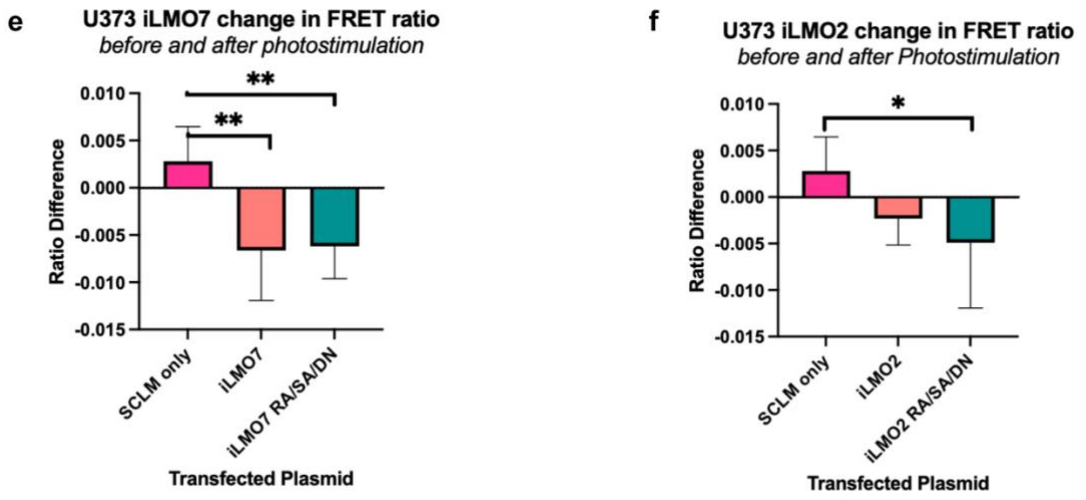

Figure 9 *- U373 SCLM Results*

a) Plate set-up for U373 96-well plate expressing SCLM. Column 1 is the non-transfected control, column 2 is the empty pcDNA3 vector + SCLM only control. Columns 4 and 6 contain the mutated forms of iLMO7 and iLMO2, respectively. b) GFP fluorescence images at 10X magnification c) SCLM ratio for the iLMO7 condition. iLMO7 showed a very significant drop in FRET ratio after photo-stimulation (marked by vertical line) compared to the SCLM-only control ($p = 0.004733$, $p< 0.01$). iLMO7 RA/SA/DN also showed a significant drop compared to the SCLM-only control ($p =0.009272$, $p < 0.01$). d) SCLM ratio for the iLMO2 condition. A significant drop in FRET ratio was found for the iLMO7 RA/SA/DN condition, as compared to the SCLM-only control ($p = 0.04027$ ($p < 0.05$). iLMO2 exhibited no significant drop in FRET ratio ($p = 0.1744$ ($p > 0.05$)). e) graph of the differences in FRET ratio before and after photo stimulation for iLMO7. f) graph of the differences in FRET ratio before and after photo stimulation for iLMO2.

Results - Intracellular pH (pHluorin2)

Similarly to SCLM, pHluorin2 is a ratiometric fluorescent protein that confers sensitivity to changes in pH. pHluorin2 is a GFP with a bimodal excitation spectrum (Mahon 2013). When a cell acidifies intracellularly, pHluorin2 shows decreased excitation around 395 nm and increased excitation around 475 nm. A greater ratio between fluorescence at these wavelengths (475 nm/395 nm) indicates greater acidification (lower pH), which is the outcome we are seeking with iLMOx expression.

The Cytation5 protocol for pHluorin2 involves an initial reading of the pHluorin2 ratio, followed by photo stimulation of iLMOx and a subsequent second reading of the pHluorin2 ratio (see Supplemental Figures, Table 3). The negative control was a co-transfected condition combining empty pcDNA3 vector + pHluorin2, which allowed for visualization of pHluorin2 expression and fluorescence quantification without any effects from iLMOx. The iLMOx RA/SA/DN mutant served as a control for NpHR activity due to its prohibitive effects on the passage of Cl^-.

Photo stimulation of iLMO2 lowers pH in HEK293FT cells.

Following photo stimulation that activated the NpHR channel of iLMO2, a significant increase in the pHluorin2 ratio was recorded in HEK293FT cells (Figure 10). This increase in ratio indicates a decrease in pH_i. One-way ANOVA testing confirmed that the increase in ratio was significant as compared to the iLMO7 RA/SA/DN and pHluorin2-only control conditions. This data indicates that the increase in pH is due to the influx of chloride through the NpHR channel.

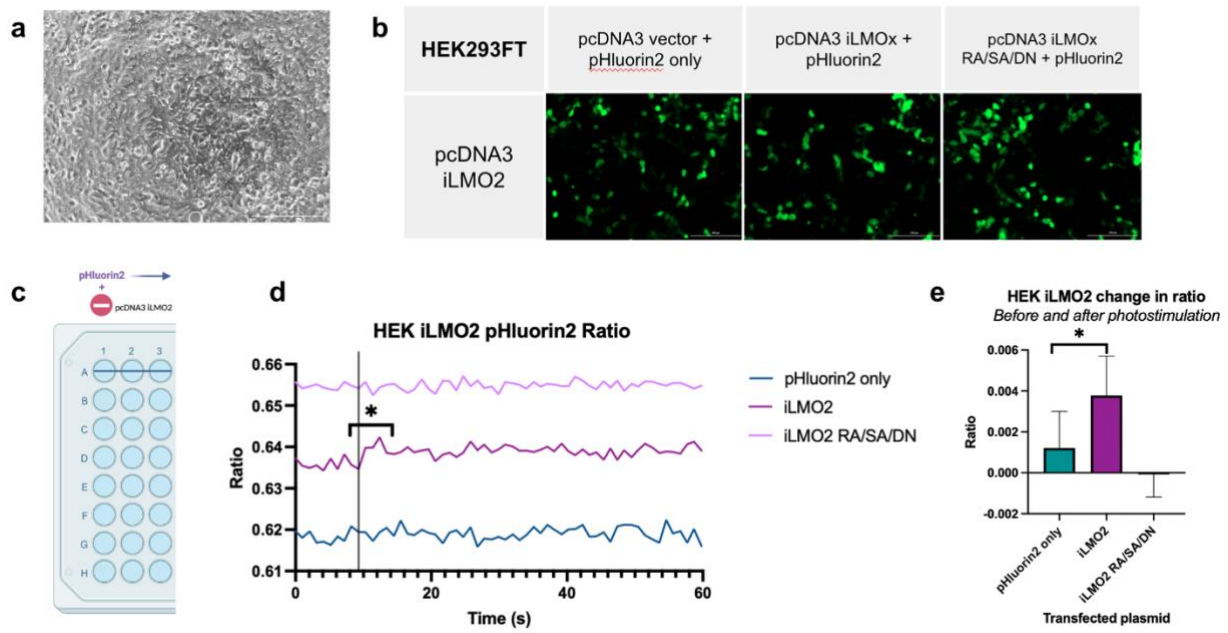

Figure 10 *- pHluorin2 in HEK293FT cells expressing iLMO2*

a) Phase contrast image of HEK293FT cells at 10X magnification. b) showing the GFP fluorescence of each experimental condition at 10X magnification. c) plate set-up for the assay, where the negative control is the pcDNA3 vector only + pHluorin2, column 2 is iLMO2, and column 3 is iLMO2 RA/SA/DN. n = 7 wells per condition. d) graph of the ratio of fluorescence (485/405 nm) for the three test conditions. The vertical line indicates when photo stimulation was applied. The increase in ratio for iLMO7 is significant via one-way ANOVA testing with Tukey HSD, $p < 0.01$. e) graph of the differences in pHluorin2 ratio before and after photo stimulation for iLMO2.

Discussion

Through the bioluminescence assay, we found that fluorescence is more robust in iLMO7 (favoring mNeonGreen), while bioluminescence is more robust in iLMO2 (favoring *Renilla* luciferase). These findings indicate that the ideal chimeric protein would actually be a hybrid combining NpHR, Renilla Luciferase, and mNeonGreen. Thinking ahead to in vivo studies, greater fluorescence facilitates confirmation of correctly localized expression. Functionally,

greater bioluminescence will be more potent when activating the NpHR light-activated chloride pump. This will increase the strength of the potential therapeutic effect on intracellular alkalization in astrocytes, an important consideration when progressing to animal studies.

After ensuring proper fluorescence, bioluminescence, and expression in vitro, chloride transport was analyzed using SCLM FRET ratios. Ultimately, iLMO7 exhibited more significant chloride influx as compared to iLMO2 in both HEK and 293FT cells. The SCLM analyses also showed that the RA/SA/DN mutation partially blocks influx of Cl^- through the NpHR channel.

After demonstrating the efficacy of chloride transport through NpHR via the SCLM experiments, we moved to explore the effects of this chloride influx on the pH_i of cells. Experiments with pHluorin2 showed a significant decrease in pH in iLMO2-expressing HEK293FT cells. This effect was not present in the RA/SA/DN mutated condition, indicating that the change in pH was a result of activation of NpHR. This result was only measured in the iLMO2 condition in HEK293FT cells.

The pHluorin2 data for U373 iLMO7, U373 iLMO2, and HEK293FT iLMO7 conditions can be found in Supplemental Figure s1. There are several reasons that could explain why pHluorin2 did not yield significant results in these other conditions, including low levels of pHluorin2 expression and fluorescence contamination from GFP components in iLMOx. In future studies, expression levels can be improved by utilizing a different and stronger promoter, such as the hybrid CAG promoter. We can also minimize contamination from GFP components by employing a shorter wavelength of excitation. We could have used 475 nm or even shorter

wavelengths, such as 420 nm (the isosbestic point of pHluorin2), for the numerator, to avoid exaction of GFP components in iLMOx. This is something that could be easily implemented in future studies with pHluorin2.

Conclusion

Overall, the results presented here indicate that iLMO7 holds promise as an agent of astrocytic homeostatic control. Fluorescence and bioluminescence were both measured at significant levels in iLMO7 and iLMO2 expressing cells. iLMO7 exhibited stronger fluorescence in vitro, while iLMO2 exhibited stronger bioluminescence in vivo. Bioluminescence and immunohistochemistry confirmed that GFAP iLMO7 expression in mice is robust and consistent, with bioluminescence levels high enough to measure externally through the skull and skin. Immunohistochemistry also confirmed that the rAAV.Astro vector effectively targets astrocytes for expression of GFAP iLMO7, a promising finding as we plan to transition fully into in vivo experimentation.

iLMO7 also demonstrated more efficient transport of Cl^- into the cell, as evident in the SCLM studies. iLMO7 consistently exhibited greater decreases in FRET ratio (corresponding to greater influx of Cl^-) in both HEK293FT and U373 cells, as compared to iLMO2. For pH measurements and the pHluorin2 results, only the HEK iLMO2 condition yielded significant results. However, this may be due to the number of confounds described in the discussion section. Further testing is needed to confirm whether or not iLMO7 has pH-altering capabilities, and how these capabilities would compare to those of iLMO2.

Moving forward, this data lays the foundation for a set of in vivo assays in mice. So far, only bioluminescence and expression of GFAP iLMO7 have been explored in mice as detailed

above. The next steps would involve visualizing changes in Cl^- and pHluorin2 fluorescence ratios before and after stimulation in the active and complex mouse brain environment. More broadly, the goal would be to induce seizures in mice using Pentylenetetrazole (PTZ), for example, and monitor any changes in seizure behavior. The goal is to minimize the duration or severity of seizures in mice, and to decrease incidence of subsequent seizure activity. Ultimately, productive results in mice could one day offer promise for a human clinical trial. In a world of limited seizure treatments ranging from medications with debilitating side effects, to invasive surgical or DBS implantation procedures, a minimally invasive opto-chemogenetic treatment offers a beacon of hope for future epilepsy treatment.

Materials and methods

Molecular Biology

To construct each plasmid, we first isolated eNL (enhanced NanoLantern (NanoLuc + mNeonGreen)) from pCAG-eLMO7 (a gift from Ute Hochgeschwender at Central Michigan University) via PCR amplification. The forward primer NotI-mNG-fwd (GCTGTGGCgGccGCCGTGTCTAAAGGAGAGGAGGATA) and the reverse primer NCS2-ER2-XhoI (GGCctcgagttacacCTcGttctcgtaGcaGaaGTTTGAAATCTTCTCGAACAG) were utilized to isolate the eNL insert, which was then ligated into pcDNA3-iLMO2 (Tung et al. 2015) using NotI and XhoI sites to produce pcDNA3 iLMO7. QuickChange (Agilent) was utilized to perform the site-directed mutagenesis needed to produce the mutant RA/SA/DN sequence following manufacturer's instructions. Primers were designed

through the QuickChange Primer Design tool available in the manufacturer's website. The iLMOx RA/SA/DN insert was ligated into the same pcDNA3-iLMO2 vector, to produce pcDNA3 iLMO7 RA/SA/DN. For the pAAV GFAP vector, pZac2.1 gfaABC1D-tdTomato (Addgene plasmid #44332) was cut at the AleI and XbaI restriction sites. Inserts were extracted from pcDNA3 iLMO7 and pcDNA3 iLMO7 RA/SA/DN via digestion with compatible SmaI and XbaI restriction enzymes. These inserts were subsequently ligated into the cut pZac2.1 gfaABC1D-tdTomato vector. After each PCR purification and vector isolation step, gel electrophoresis was used to confirm that the correctly sized gene sequences had been isolated. Ligation reacitons were transformed into E. coli and subsequently purified via miniprep (Takara Bio NeculeoSpin Plasmid). To confirm the identity of each correct final plasmid sequence, plasmids underwent restriction digestion and subsequent gel electrophoresis. Following in-house confirmation, the final plasmids were sent off for third party sequencing (Plasmidsaurus).

	iLMO7	**iLMO7 RA/SA/DN**	**iLMO2**	**iLMO2 RA/SA/DN**
pcDNA3	pcDNA3 iLMO7	pcDNA3 iLMO7 RA/SA/DN	pcDNA3 iLMO2	pcDNA3 iLMO2 RA/SA/DN
pAAV GFAP	pAAV GFAP iLMO7	pAAV GFAP iLMO7 RA/SA/DN		

Table 1 – *Plasmid and vector combinations used during experiments.*

pcDNA3 is a mammalian expression vector utilized across all mammalian cell types. pAAV GFAP confers the astrocyte-specific GFAP promoter.

Cell culture

HEK293FT cells and U373 cells were cultured and passaged in Dulbecco's Modified Eagle's Medium-high glucose (DMEM) with an added 10% FBS, 1% PenStrep, and 1% L-glutamine. Cells were incubated in humidified conditions at 37 degrees Celsius and 5% CO_2. For cell-based assays, freshly passaged cells were aliquoted into 96-well plates (100 uL per well).

Transfection

After 24 hours to achieve confluency of about 80%, each 96-well plate was transfected with the desired lipofection treatment condition. Both HEK293FT cells and U373 cells were transfected using Lipofectamine 3000 (0.2 ug DNA per well). 10 uL of lipofection cocktail were added to the 100 uL of media present per well of a 96 well plate. Cells were given 1-2 days to grow/adhere to the 96-well plate prior to transfection. Cells were exposed to the transfection cocktail overnight, typically for around 24 hours, prior to the final plate reading data collection.

rAAV production

rAAV was produced in-house using our standard protocol. In brief, HEK293FT cells were transfected with transfer (one of pAAV GFAP described above), helper, and capsid/replicase plasmid (pAAV9.PHP.Astro; a gift from Viviana Gradinaru, Caltech)

using the calcium-phosphate method. The cells and the media were harvested 3 days later and rAAV was purified and concentrated through ultracentrifugation in OptiPrep density gradient and filtration/dialysis membrane column. rAAV was resuspended in sterile PBS and the titer was determined by quantitative PCR.

Mouse protocol

Four mouse pups were given bilateral intracerebroventricular injections of the viral vector rAAV.Astro/GFAP iLMO7 (1 μL each = 1.9×10^{11} viral particles) shortly after birth (Kim et al. 2014). rAAV.Astro is a recombinant viral vector that targets astrocytes in mice. After three weeks, in vivo bioluminescence was measured in injected mice. Prior to imaging, the fur was shaved from the head for better external visualization of bioluminescence in the brain. Mice were anesthetized with isoflurane (3%) during both the injection and subsequent imaging period. A dose of 10 mg/kg CTZ was injected intraperitoneally, and after five minutes, the anesthetized mice were placed in a dark box for imaging. Bioluminescence images were taken using a luminescence imager (Fuji-LAS 3000) once per minute for a total of 80 minutes. Subsequent analyses with ImageJ yielded a time-dependent trace of the bioluminescence signal from each mouse.

Histology

Prior to immunohistochemistry, the mouse was perfused with a fixative (4% paraformaldehyde in PBS). Afterward, their brain was extracted, placed into cryoprotectant (30% sucrose in PBS) overnight, and frozen. A cryostat was utilized to slice brains at a thickness of 30 microns. Slices were then immunostained against GFAP

(primary antibody was an anti-rabbit antibody against mouse GFAP, secondary antibody was anti-rabbit antibody conjugated with AlexaFluor 594 to mark GFAP). Slices were mounted onto glass slides and coverslipped with VectaShield mounting media containing DAPI. Green fluorescence was marked in iLMO7 due to the presence of mNeonGreen fluorescent protein.

Cell Plate Assays and Exclusion

Cell Plate reading assays were carried out using the Cytation5 Cell Imaging Multimode reader. The plate compartment was maintained at 37 degrees Celsius and 5% CO_2 to ensure cellular wellbeing, as plate reads often require multiple hours. Prior to measurements, phase contrast and GFP photos were taken with the Cytation5 microscope. Due to the effects of photobleaching, wells that had been photographed were excluded from the imaging assays that followed (the first row). Specific steps for each protocol are detailed in the Supplemental Figures section, Table s1-s3.

Statistical analysis

All analysis and statistical testing were performed using Prism (GraphPad). For bioluminescence statistics, an unpaired t-test was utilized with FDR (False Discovery Rate) and Two-stage step-up (Benjamini, Krieger, and Yekutieli). For SCLM and pHluorin2 analysis, a one-way ANOVA with Tukey HSD was utilized to discern significant differences between group data.

Supplemental Figures

Fluorescence/Bioluminescence
Temperature: Setpoint 37 °C
Read: (F) 479, 520 nm
Plate Out, In - Add CTZ
Read: (L) Lum

Table s1*: Bioluminescence protocol, as programmed in Cytation5*

FRET (flashing)
Temperature: Setpoint 37 °C
Well mode Start Kinetic [Run 0:13.00, Interval 0:01.40] Read: FRET (F) 430, 491, 430, 541 nm End Kinetic
End Mode
Read: Texas Red 586, 647, Texas Red 586, 647[2], Texas Red 586, 647[3], Texas Red 586, 647[4], Texas Red 586, 647[5], Texas Red 586, 647[6]
Well mode Start Kinetic [Run 1:09.00, Interval 0:01.40] Read: FRET (F) 430, 491, 430, 541 nm

End Kinetic
End Mode

Table s2: *SCLM protocol, as programmed in Cytation5*

Texas Red is the filter cube utilized for imaging at this wavelength. FRET wavelengths are specific for the SCLM protein. The Texas Red light was used between Well Mode reads to activate the NpHR chloride pump. Fluorescence reads were obtained in the Well Mode steps before and after this optogenetic activation.

pHluorin2 (flashing)
Temperature: Setpoint 37 °C
Well mode Start Kinetic [Run 0:10.00, Interval 0:01.03] Read: FRET (F) 405, 510, 485, 510 nm End Kinetic
End Mode
Read: (F) 584, 625, 584, 625 [2], 584, 625 [3], 584, 625 [4], 584, 625 [5], 584, 625 [6]
Well mode Start Kinetic [Run 0:51.00, Interval 0:01.03] Read: FRET (F) 405, 510, 485, 510 nm End Kinetic

End Mode

Table s3: *pHluorin2 protocol, as programmed in Cytation5*

FRET wavelengths are specific for the pHluorin2 protein.

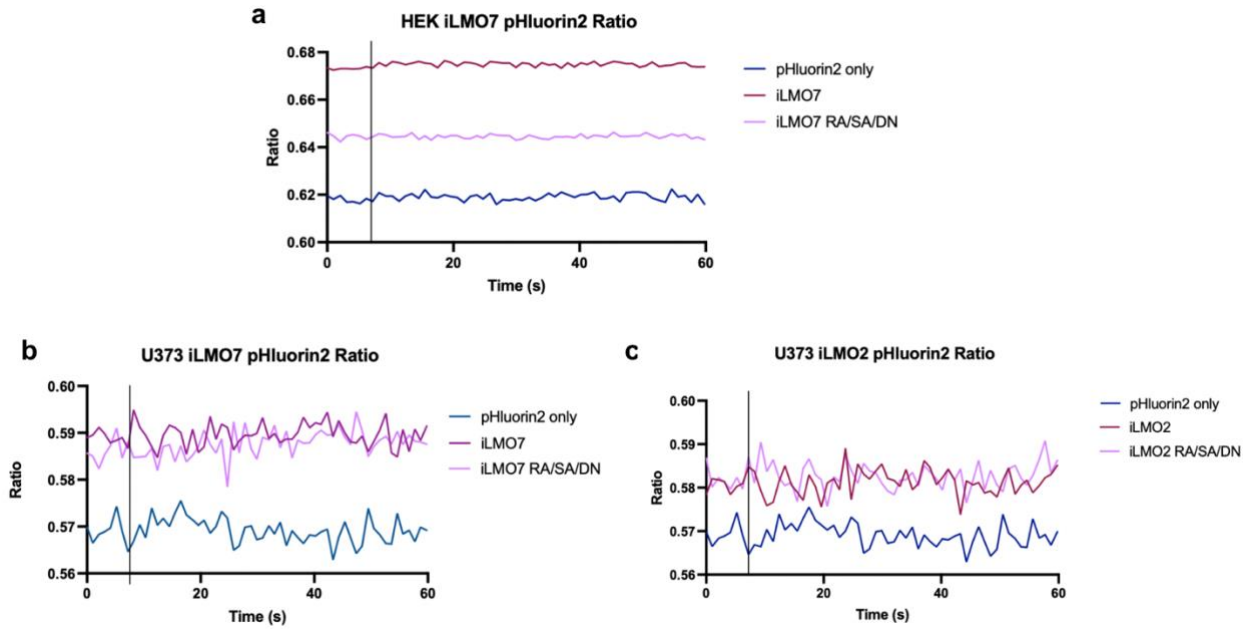

Figure 1s *– pHluorin2 data for HEK293FT iLMO7, U373 iLMO7, and U373 iLMO2 conditions a) HEK iLMO7 results, showing no significant change in pHluorin2 ratio after photo stimulation (marked by the vertical line), n = 7 wells per condition. b-c) U373 pHluorin2 data, no significant changes in pH after photo stimulation. Data is considerably noisier compared to HEK results, indicating lower reliability of U373 cell line for pHluorin2 assays.*

References

Bellot-Saez, A., Kékesi, O., Morley, J. W., & Buskila, Y. (2017). Astrocytic modulation of neuronal excitability through K + spatial buffering. *Neuroscience & Biobehavioral Reviews*, *77*, 87–97. https://doi.org/10.1016/j.neubiorev.2017.03.002

Berglund, K., Clissold, K., Li, H. E., Wen, L., Park, S. Y., Gleixner, J., Klein, M. E., Lu, D., Barter, J. W., Rossi, M. A., Augustine, G. J., Yin, H. H., & Hochgeschwender, U. (2016). Luminopsins integrate opto- and Chemogenetics by using physical and biological light sources for opsin activation. *Proceedings of the National Academy of Sciences*, *113*(3). https://doi.org/10.1073/pnas.1510899113

Berglund, K., Wen, L., Dunbar, R. L., Feng, G., & Augustine, G. J. (2016). Optogenetic visualization of presynaptic tonic inhibition of cerebellar parallel fibers. *The Journal of Neuroscience*, *36*(21), 5709–5723. https://doi.org/10.1523/jneurosci.4366-15.2016

Biorender. BioRender App. (n.d.). Retrieved April 10, 2023, from https://app.biorender.com/

Bittner, C. X., Valdebenito, R., Ruminot, I., Loaiza, A., Larenas, V., Sotelo-Hitschfeld, T., Moldenhauer, H., San Martín, A., Gutiérrez, R., Zambrano, M., & Barros, L. F. (2011). Fast and reversible stimulation of astrocytic glycolysis by K+ and a delayed and persistent effect of glutamate. *The Journal of Neuroscience*, *31*(12), 4709–4713. https://doi.org/10.1523/jneurosci.5311-10.2011

Chen, X., Kumar, R. S., Ding, X., & Gradinaru, V. (2019). AAV engineering by multiplexed-create selection and rational peptide insertion yields variants with enriched targeting of CNS astrocytes upon systemic delivery. *Session 612 - Optic Methods: Development and Applications*.

Chen, X., Ravindra Kumar, S., Adams, C. D., Yang, D., Wang, T., Wolfe, D. A., Arokiaraj, C. M., Ngo, V., Campos, L. J., Griffiths, J. A., Ichiki, T., Mazmanian, S. K., Osborne, P. B., Keast, J. R., Miller, C. T., Fox, A. S., Chiu, I. M., & Gradinaru, V. (2022). Engineered aavs for non-invasive gene delivery to rodent and non-human Primate Nervous Systems. *Neuron*, *110*(14). https://doi.org/10.1016/j.neuron.2022.05.003

CO2 sensors for cell culture incubators, patient care, Health Studies. Gaslab.com. (n.d.). Retrieved March 23, 2023, from https://gaslab.com/blogs/articles/co2-sensors-incubators-health-life-sciences#:~:text=Research%20has%20shown%20that%20a,the%20equivalent%20of%2050%2C000ppm.

de Curtis, M., Uva, L., Gnatkovsky, V., & Librizzi, L. (2018). Potassium dynamics and seizures: Why is potassium ictogenic? *Epilepsy Research*, *143*, 50–59. https://doi.org/10.1016/j.eplepsyres.2018.04.005

Du, M., Li, J., Wang, R., & Wu, Y. (2016). The influence of potassium concentration on epileptic seizures in a coupled neuronal model in the hippocampus. *Cognitive Neurodynamics*, *10*(5), 405–414. https://doi.org/10.1007/s11571-016-9390-4

EbrahimAmini, A., Mylvaganam, S., Bazzigaluppi, P., Khazaei, M., Velumian, A., Stefanovic, B., & Carlen, P. L. (2021). In vivo neocortical [k]o modulation by targeted stimulation of astrocytes. *International Journal of Molecular Sciences*, *22*(16), 8658. https://doi.org/10.3390/ijms22168658

Elorza-Vidal, X., Gaitán-Peñas, H., & Estévez, R. (2019). Chloride channels in astrocytes: Structure, roles in brain homeostasis and implications in disease. *International Journal of Molecular Sciences*, *20*(5), 1034. https://doi.org/10.3390/ijms20051034

England, C. G., Ehlerding, E. B., & Cai, W. (2016). NanoLuc: A small luciferase is brightening up the field of bioluminescence. *Bioconjugate Chemistry*, *27*(5), 1175–1187. https://doi.org/10.1021/acs.bioconjchem.6b00112

Herstel, L. J., Peerboom, C., Uijtewaal, S., Selemangel, D., Karst, H., & Wierenga, C. J. (2022). Using SuperClomeleon to measure changes in intracellular chloride during development and after early life stress. https://doi.org/10.1101/2022.10.06.511115

Hertz, L., Xu, J., Song, D., Yan, E., Gu, L., & Peng, L. (2013). Astrocytic and neuronal accumulation of elevated extracellular K+ with a 2/3 k+/na+ flux ratio—consequences for energy metabolism, osmolarity and higher brain function. *Frontiers in Computational Neuroscience*, *7*. https://doi.org/10.3389/fncom.2013.00114

Kim, J.-Y., Grunke, S. D., Levites, Y., Golde, T. E., & Jankowsky, J. L. (2014). Intracerebroventricular viral injection of the neonatal mouse brain for persistent and widespread neuronal transduction. *Journal of Visualized Experiments*, (91). https://doi.org/10.3791/51863

Kinboshi, M., Ikeda, A., & Ohno, Y. (2020). Role of astrocytic inwardly rectifying potassium (KIR) 4.1 channels in epileptogenesis. *Frontiers in Neurology*, *11*. https://doi.org/10.3389/fneur.2020.626658

Kuner, T., & Augustine, G. J. (2000). A genetically encoded ratiometric indicator for chloride. *Neuron*, *27*(3), 447–459. https://doi.org/10.1016/s0896-6273(00)00056-8

Libretexts. (2023, January 30). *Fluorescence Resonance Energy Transfer*. Chemistry LibreTexts. Retrieved March 23, 2023, from https://chem.libretexts.org/Bookshelves/Physical_and_Theoretical_Chemistry_Textbook_Maps/Supplemental_Modules_(Physical_and_Theoretical_Chemistry)/Fundamentals/Fluorescence_Resonance_Energy_Transfer

Lipofectamine™ 3000 transfection reagent. Thermo Fisher Scientific - US. (n.d.). Retrieved March 23, 2023, from https://www.thermofisher.com/order/catalog/product/L3000015

Mahon, M. J. (2011). Phluorin2: An enhanced, ratiometric, ph-sensitive green florescent protein. *Advances in Bioscience and Biotechnology*, *02*(03), 132–137. https://doi.org/10.4236/abb.2011.23021

Makara, J. K., Rappert, A., Matthias, K., Steinhäuser, C., Spät, A., & Kettenmann, H. (2003). Astrocytes from mouse brain slices express CLC-2-mediated CL− currents regulated during development and after injury. *Molecular and Cellular Neuroscience*, *23*(4), 521–530. https://doi.org/10.1016/s1044-7431(03)00080-0

Onodera, M., Meyer, J., Furukawa, K., Hiraoka, Y., Aida, T., Tanaka, K., Tanaka, K. F., Rose, C. R., & Matsui, K. (2021). Exacerbation of epilepsy by Astrocyte alkalization and Gap Junction uncoupling. *The Journal of Neuroscience*, *41*(10), 2106–2118. https://doi.org/10.1523/jneurosci.2365-20.2020

PDRIVE-GFAP. InvivoGen. (2021, January 13). Retrieved March 23, 2023, from https://www.invivogen.com/pdrive-gfap#:~:text=GFAP%20promoter%20(Astrocytes)%20in%20pDRIVE,found%20almost%20exclusively%20in%20astrocytes

Ruminot, I., Schmälzle, J., Leyton, B., Barros, L. F., & Deitmer, J. W. (2017). Tight coupling of astrocyte energy metabolism to synaptic activity revealed by genetically encoded fret nanosensors in hippocampal tissue. *Journal of Cerebral Blood Flow & Metabolism*, *39*(3), 513–523. https://doi.org/10.1177/0271678x17737012

Shimada, T., & Yamagata, K. (2018). Pentylenetetrazole-induced kindling mouse model. *Journal of Visualized Experiments*, (136). https://doi.org/10.3791/56573-v

Snapp, E. L., Altan, N., & Lippincott-Schwartz, J. (2003). Measuring Protein Mobility by photobleachinggfpchimeras in living cells. *Current Protocols in Cell Biology*, *19*(1). https://doi.org/10.1002/0471143030.cb2101s19

Suzuki, K., Kimura, T., Shinoda, H., Bai, G., Daniels, M. J., Arai, Y., Nakano, M., & Nagai, T. (2016). Five colour variants of bright luminescent protein for real-time multicolour bioimaging. *Nature Communications*, *7*(1). https://doi.org/10.1038/ncomms13718

Swietach, P., Rossini, A., Spitzer, K. W., & Vaughan-Jones, R. D. (2007). H+ ion activation and inactivation of the ventricular gap junction. *Circulation Research*, *100*(7), 1045–1054. https://doi.org/10.1161/01.res.0000264071.11619.47

Theparambil, S. M., Hosford, P. S., Ruminot, I., Kopach, O., Reynolds, J. R., Sandoval, P. Y., Rusakov, D. A., Barros, L. F., & Gourine, A. V. (2020). Astrocytes regulate brain extracellular ph via a neuronal activity-dependent bicarbonate shuttle. *Nature Communications*, *11*(1). https://doi.org/10.1038/s41467-020-18756-3

Theparambil, S. M., Ruminot, I., Schneider, H.-P., Shull, G. E., & Deitmer, J. W. (2014). The electrogenic sodium bicarbonate cotransporter nbce1 is a high-affinity bicarbonate carrier

in cortical astrocytes. *The Journal of Neuroscience*, *34*(4), 1148–1157. https://doi.org/10.1523/jneurosci.2377-13.2014

Tung, J. K., Berglund, K., & Gross, R. E. (2016). Optogenetic approaches for controlling seizure activity. *Brain Stimulation*, *9*(6), 801–810. https://doi.org/10.1016/j.brs.2016.06.055

Tung, J. K., Berglund, K., Gutekunst, C.-A., Hochgeschwender, U., & Gross, R. E. (2016). Bioluminescence imaging in live cells and animals. *Neurophotonics*, *3*(02), 1. https://doi.org/10.1117/1.nph.3.2.025001

Tung, J. K., Gutekunst, C.-A., & Gross, R. E. (2015). Inhibitory luminopsins: Genetically-encoded bioluminescent opsins for versatile, scalable and hardware-independent optogenetic inhibition. *Scientific Reports*, *5*(1). https://doi.org/10.1038/srep14366

Tønnesen, J., Sørensen, A. T., Deisseroth, K., Lundberg, C., & Kokaia, M. (2009). Optogenetic control of epileptiform activity. *Proceedings of the National Academy of Sciences*, *106*(29), 12162–12167. https://doi.org/10.1073/pnas.0901915106

Wagnon, J. L. (2021). Back to basics: A role for astrocyte alkalization in Epileptogenesis. *Epilepsy Currents*, *21*(4), 298–299. https://doi.org/10.1177/15357597211018687

Wallraff, A., Köhling, R., Heinemann, U., Theis, M., Willecke, K., & Steinhäuser, C. (2006). The impact of astrocytic gap junctional coupling on potassium buffering in the hippocampus. *The Journal of Neuroscience*, *26*(20), 5438–5447. https://doi.org/10.1523/jneurosci.0037-06.2006

Ying, T., Grayden, D. B., Burkitt, A. N., & Kameneva, T. (2015). An increase in the extracellular potassium concentration can cause seizures. *BMC Neuroscience*, *16*(S1). https://doi.org/10.1186/1471-2202-16-s1-p113